Computational Modeling of Adiabatic Heating in Triaxially Braided Polymer Matrix Composites Subjected to Impact Loading via a Subcell Based Approach

Christopher Sorini[1], Aditi Chattopadhyay[1], and Robert K. Goldberg[2]
[1]*Arizona State University, Tempe, AZ, USA*
[2]*NASA Glenn Research Center, Cleveland, OH, USA*

Abstract

The high rate deformation of polymer matrix composites is often accompanied by significant local adiabatic heating; in the case of ballistic impact loading, heat is generated locally within the polymer matrix due to the conversion of plastic work to heat, but the rapid nature of the event does not allow sufficient time for heat transfer to occur. In this work, a user-defined material subroutine implemented into LS-DYNA® to facilitate the analysis of triaxially braided polymer matrix composites subjected to impact loading, including the effects of heat generation due to high rate inelastic deformation of the polymer matrix, is discussed. To approximate the triaxially braided architecture in finite element models in a computationally efficient manner, a subcell-based modeling approach is utilized whereby the mesoscale repeating unit cell of the triaxial braid is discretized in-plane into an assemblage of subcells. Each mesoscale subcell is approximated as a unique composite laminate with stacking sequence determined from the braid architecture and unidirectional layer thicknesses and fiber volume fractions determined from optical micrographs. Each laminate is modeled in LS-DYNA as a layered thick shell element, where integration point strain increments are taken as volume averaged strain increments applied to a doubly-periodic repeating unit cell with one fiber and three matrix microscale subcells. The generalized method of cells micromechanics theory is utilized to localize the globally applied strains to the constituent level to determine the local strains and stresses as well as the global response of the doubly-periodic repeating unit cell via homogenization. An existing unified pressure dependent viscoplastic constitutive model that was previously extended by the authors to nonisothermal conditions is utilized to model the rate, temperature, and pressure dependent polymer matrix. In the polymer constitutive model, the inelastic strain rate tensor components have been modified to explicitly depend on temperature; strain rate and temperature dependent shifts in matrix elastic properties are determined by shifting dynamic mechanical analysis data with the integration point effective strain rate. Since the subroutine is micromechanical in nature, constitutive models are only applied at the lowest (micro) length scale. Local temperature rises in the polymer matrix due to inelastic deformation are computed at the microscale via the heat energy equation, assuming adiabatic conditions. Simulations of quasi-static straight-sided coupon tests and flat panel impact tests on a representative [0°/60°/–60°] triaxially braided composite material system are conducted to validate the subcell methodology and study the effects of adiabatic heating on the simulated impact response. Time histories of simulated and experimentally measured out-of-plane displacement profiles during the impact event are compared; good agreement is found between experiments and simulations. Simulation results indicate significant internal temperature rises due to the conversion of plastic work to heat in an impact event.

Introduction

Polymer matrix composites (PMCs) are often used to fabricate aerospace structural components required to maintain structural integrity in the instance of high energy impact loading, such as jet engine fan blade containment systems subjected to blade-out. The high specific strength and stiffness as well as the delamination resistance of braided tow architectures make PMCs attractive over monolithic materials for such applications. However, the development of predictive computational models for PMCs under impact loading conditions is impeded by the inherent material heterogeneity and anisotropy, multiscale nature, and the complex interaction between the fiber reinforcement and the strain rate, temperature, and pressure dependent polymer matrix. Additionally, high rate deformation is not isothermal; as the rate of deformation increases, the thermodynamic condition transitions from isothermal to adiabatic. In the case of ballistic impact events, heat is generated locally within the polymer matrix due to the conversion of plastic work to heat, but the rapid nature of the impact event

does not allow sufficient time for heat transfer to occur. Local temperature rises, which could be greater than the matrix glass transition temperature [1], can lead to substantial thermal softening and subsequent localization if softening effects outweigh strain and strain rate hardening effects [2], and therefore must be accounted for in computational models. Thus, to expedite the development and certification timelines of new impact resistant PMC material systems and structures, it is necessary to develop robust and computationally efficient models to gain insight into the deformation, progressive damage, and failure response of PMCs subjected to dynamic loading conditions.

Though several constitutive models exist in LS-DYNA [3] for composite material analysis, many of them have drawbacks that deem them incapable of modeling all the phenomena of interest: complex interaction between the constituent materials (fiber and matrix); adiabatic heating and subsequent thermal softening in the rate, temperature, and pressure dependent polymer matrix; material nonlinearity due to a combination of matrix progressive damage and inelasticity; ultimate failure. To account for the interaction between constituent materials at the microscale, a micromechanics-based constitutive model must be used. However, the only micromechanics-based composite model in LS-DYNA is MAT_235 (Micromechanics Dry Fabric). This model was developed by Tabiei and Ivanov [4, 5] to model the elastic response of loose dry fabric, including yarn reorientation effects, not textile composites [6]. The MAT_058 and MAT_158 (Laminated Composite Fabric and Rate Sensitive Composite Fabric) material models are continuum-level models based on the work of Matzenmiller [7]. They are suitable for modeling woven fabric laminates and are capable of simulating nonlinear behavior in all material directions. These models have been used successfully in impact analyses [8-10], though failure strains determined from quasi-static coupon tests often need to be artificially increased to match experimentally measured ballistic limits. In MAT_058 and MAT_158, all material nonlinearity is due to damage evolution rather than a combination of inelasticity and damage; since plastic strains are not computed, these models are incapable of simulating temperature rises due to the conversion of plastic work to heat. Though developed to model the rate dependent response of metals, an orthotropic material model that *is* capable of modeling temperature rises due to inelastic deformation is MAT_264 (Tabulated Johnson Cook Orthotropic Plasticity), which is based on the Johnson-Cook plasticity model. Since plastic deformation in metals is assumed to be deviatoric, this model is not applicable to the analysis of PMCs, for which the matrix response exhibits a significant dependence on hydrostatic pressure. Schweizerhoff [11] discusses the benefits and drawbacks of LS-DYNA composite material models in more detail.

Since none of the composite material models currently available in LS-DYNA are capable of modeling all the phenomena of interest, the authors have developed a micromechanics-based user-defined material subroutine (UMAT) to be used in the context of a subcell-based approach for modeling the architecturally dependent impact response of braided PMCs with complex fiber architectures, accounting for local adiabatic heating effects. It should be noted that the current version of the UMAT does not yet account for progressive damage and failure. The organization of the paper is as follows. Details of the developed UMAT are presented first, including the nonisothermal polymer constitutive model used to model the strain rate, temperature, and pressure dependent polymer matrix. A means of determining the elastic properties of the polymer matrix at various strain rates and temperatures based on dynamic mechanical analysis (DMA) data is described, as well as how temperature rises due to plastic deformation are computed in the incremental explicit finite element simulations. A brief discussion of the generalized method of cells (GMC) micromechanics theory [12], which the UMAT is based upon, is discussed. Next, the subcell methodology [9, 13-19] is described and applied to a representative triaxially braided composite material system. Straight-sided quasi static coupon tests as well as a flat panel impact test are simulated with the developed UMAT and compared to available experimental data. A discussion of the simulation results is presented followed by concluding remarks and plans for future work.

User Material Subroutine

Polymer Constitutive Model

As aforementioned, the constitutive behavior of polymeric materials is highly strain rate, temperature, and pressure dependent; as such, the polymer constitutive model must incorporate these effects. The unified viscoplastic constitutive model of Bodner and Partom [20], which was originally developed to model the high temperature viscoplastic response of metals, was subsequently modified by Goldberg [21] to incorporate hydrostatic stress effects, which are known to be significant in polymers. In previous work by the authors [22], the said viscoplastic model [21] was extended to nonisothermal conditions by introducing temperature dependent state variables and by modifying inelastic strain rate tensor components to depend explicitly on temperature. The model is employed in this work to describe the strain rate, temperature, and pressure dependent response of the polymer matrix. Strains are assumed to be infinitesimal and, as such, the total strains can be additively decomposed into their elastic, inelastic, and thermal parts, respectively. A brief overview of the model governing equations is as follows; for more details, the reader is referred to [21] and [22].

$$\dot{\epsilon_{ij}^I} = 2D_0 \exp\left(\frac{-1}{2}\left(\frac{\bar{Z}}{T\sigma_e}\right)^{2n}\right)\left(\frac{S_{ij}}{2\sqrt{J_2}} + \alpha\delta_{ij}\right) \tag{1}$$

$$\sigma_e = \sqrt{3J_2} + \sqrt{3}\alpha\sigma_{kk} \tag{2}$$

$$\dot{\alpha} = q(\alpha_1 - \alpha)\,\dot{e_e^I} \tag{3}$$

$$\bar{Z} = \bar{Z}_1 - (\bar{Z}_1 - \bar{Z}_0)\exp(-qe_e^I) \tag{4}$$

$$\dot{e_e^I} = \sqrt{\frac{2}{3}\dot{e_{ij}^I}\dot{e_{ij}^I}} \tag{5}$$

In equations 1-5, D_0 is a model constant that represents the maximum inelastic strain rate, n is a model constant that controls strain rate sensitivity, $\bar{Z}$ is a time and temperature dependent state variable that represents the resistance to internal stress at a given temperature (captures strain hardening), q is a model constant that controls the hardening rate, α is a time dependent state variable that controls the influence of hydrostatic stress effects, T is the absolute (Kelvin) temperature, σ_e is the effective stress, S_{ij} are the components of the deviatoric stress tensor, J_2 is the second invariant of the deviatoric stress tensor, and δ_{ij} is the Kronecker delta, and $\dot{e_e^I}$ is the effective deviatoric inelastic strain rate. A dot superscript denotes a time derivative and the summation convention is assumed to apply for repeated indices. Rather than requiring a defined yield stress, rate and temperature dependent yield is captured by the evolution of the state variables $\bar{Z}$ and α with the effective deviatoric inelastic strain rate from their initial values ($\bar{Z}_0$ and α_0) to their final values (α_1 and $\bar{Z}_1$). An explicit forward Euler integration scheme is used to integrate equations 1 and 3 forward in time to determine the current values of the inelastic strain tensor components and the hydrostatic state variable.

To determine the elastic properties of the polymer matrix across a range of temperatures and strain rates, a time-temperature shifting methodology, similar to the decompose-shift-reconstruct (DSR) method developed by Mulliken and Boyce [23], is employed. Temperature and strain rate dependent shifts in elastic moduli are computed based on DMA data from tests conducted by Gilat et al. [24] on neat resin at various frequencies and

temperatures. Since the frequency at which a DMA test is conducted corresponds to a particular strain rate (depending on specimen geometry), strain rate dependent shifts in moduli can be determined by conducting DMA tests at multiple frequencies. A schematic showing the shifting of the shear storage modulus versus temperature curve (obtained via DMA testing) with effective strain rate is shown in Figure 1. In this work, the shear modulus is assumed to be equal to the shear storage modulus and Poisson's ratio is assumed to be independent of temperature [25].

The heat energy equation, which governs the interdependence of mechanical deformation and spatial-temporal temperature change, is expressed as follows:

$$k\nabla^2 T - \alpha_M(3\lambda + 2\mu)T\dot{\varepsilon}^e_{kk} + \beta\boldsymbol{\sigma}:\dot{\boldsymbol{\varepsilon}}^{\boldsymbol{I}} = \rho C\dot{T}, \tag{6}$$

where k is the thermal conductivity, T is the absolute temperature, α_M is the coefficient of thermal expansion (CTE), λ and μ are Lame's constants, ε^e_{kk} is the elastic volumetric strain, $\boldsymbol{\sigma}$ is the Cauchy stress tensor, $\boldsymbol{\varepsilon}^I$ is the inelastic strain tensor, ρ is the density, C is the specific heat, and β is the inelastic heat fraction, which represents the proportion of plastic work converted to heat. For adiabatic conditions, the thermoelastic and conduction terms are often considered negligible compared to the thermoplastic term [25-27]. Under this assumption, the heat energy reduces to the following:

$$\beta\boldsymbol{\sigma}:\dot{\boldsymbol{\varepsilon}}^{\boldsymbol{I}} = \rho C\dot{T}. \tag{7}$$

Assuming the inelastic heat fraction is known (either experimentally measured or assumed), equation 7 can be solved for $\dot{T}$ and integrated using a forward Euler integration scheme to compute temperature rises due to plastic deformation at each timestep in an explicit finite element simulation.

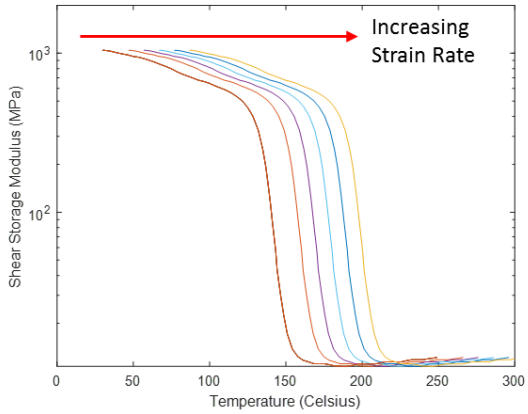

Figure 1: Illustration of the shifting of DMA data with strain rate.

Micromechanics

The developed UMAT is based on the doubly-periodic GMC micromechanics theory [12]. By assuming a first order subcell displacement field, and by applying continuity of displacements and tractions between adjacent subcells and unit cells, the doubly periodic GMC can accurately predict subcell stresses and strains, as well as the effective homogenized repeating unit cell (RUC) response, based on the globally applied RUC strains and the material properties, arrangement, and relative volume fractions of the constituent materials. A four subcell RUC was used for the UMAT implementation to reduce the number of history variables (since it is

useful to store subcell stresses, strains, etc.) and computational cost. The RUC consists of one fiber and three matrix subcells, as illustrated in Figure 2, where V_f denotes the RUC fiber volume fraction. The fiber is assumed to be transversely isotropic in the 2-3 plane and exhibit linear elastic behavior. The effect of temperature on the fiber properties has not been considered in this work. As mentioned in the previous section, the viscoplastic strain rate, temperature, and pressure dependent constitutive equations are implemented within the GMC micromechanics model to simulate the nonlinear response of the three matrix subcells, including the effects of adiabatic heating due to inelastic deformation. It should be emphasized that, at each finite element integration point, the strain increments passed into the UMAT are taken to be the RUC average strain increments; these strains are then used to determine the total RUC strains, subcell strains, subcell stresses, and global RUC stresses via volume averaging of the subcell stresses. The volume averaged stresses are then taken as the integration point stresses for the particular timestep. The reader is referred to References 28-31 for additional details regarding the GMC theory and formulation.

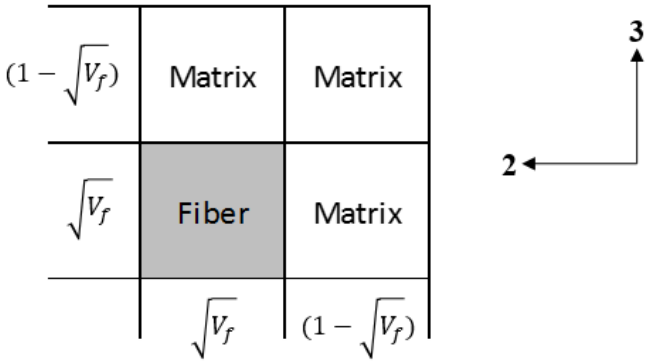

Figure 2: Schematic of four subcell doubly-periodic RUC.

Subcell Methodology

The material system under investigation in this study is a T700/Epon 862 [0°/60°/–60°] triaxially braided composite. Epon 862 (E862) is a low viscosity, high flow thermoset epoxy resin [8] and T700 is a high strength carbon fiber manufactured by Toray. The triaxially braided carbon fiber preform (no resin), shown in Figure 3, consists of 24K tows in the axial direction (red arrow) and 12K tows in the bias/braider (blue arrows) directions. The triaxially braided architecture is known to be resistant to failures driven by interlaminar stresses [32] and the 60° braid angle is known to approximately exhibit quasi-static in-plane properties. It should be noted that, due to the relatively large RUC compared to the size of structural components (dimensions shown in Figure 3b), the deformation and progressive damage behavior of the triaxial braid is a function of the material architecture. To account for the material heterogeneity at the highest analysis length scale, a subcell-based approach [9, 13-19] is utilized, whereby the braided composite RUC is discretized into an assemblage of adjacent laminated composites, with stacking sequences determined from the braid architecture. The subcell methodology, illustrated in Figures 3a-c, consists of identifying the braided composite RUC and discretizing it in-plane into a series of subcells depending on the presence of axial and/or braider tows or lack thereof. The subcells are then discretized through their thicknesses into an approximation of unidirectional (UD) plies with layups determined by the braid architecture. It can be seen in Figure 3d that subcells A and C have antisymmetric stacking sequences whereas subcells B and D have symmetric stacking sequences. The RUC discretization shown in Figure 3d was developed by [18] and is known as the absorbed matrix model (AMM) because pure matrix layers are not explicitly modeled; braider plies are assumed to be a homogenized representation of braider tows and surrounding pure matrix regions [17, 18].

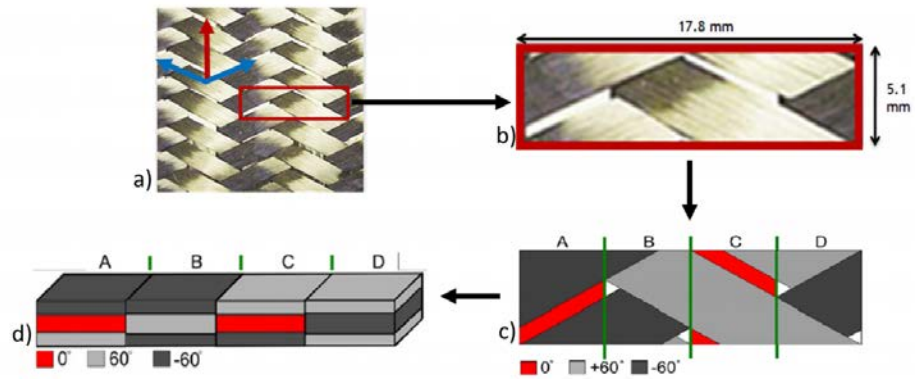

Figure 3: a) RUC identification; b) Enlarged image of identified RUC with dimensions shown; c) Identification of four adjacent subcell regions; d) Discretization of each subcell through its thickness into an approximation of unidirectional plies.

The UD ply thicknesses and fiber volume fractions, shown in Table 1, were determined via optical microscopy, knowledge of the overall composite fiber volume fraction of 56%, and the microscopy-informed assumption that subcells A and C each have a fiber volume fraction of 60%. The total height of the RUC is 0.53 mm; the widths of subcells A/C and B/D are 5.626 mm and 3.264 mm, respectively, resulting in a total RUC width of 17.78 mm. Figure 4 shows a coarse finite element mesh of the triaxially braided RUC, where each subcell has been modeled as a single thick shell element with three through thickness integration points, each corresponding to a UD ply. Thick shells have the advantage over 2D shell elements in that they are able to admit a full 3D stress state, which is crucial in impact problems, where large transverse normal and shear stresses are expected. All material properties and model constants used in the analyses to follow have been determined in previous work [19, 22] and are shown in Tables 1, 2, and 3.

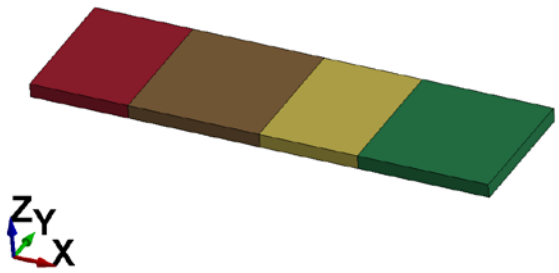

Figure 4: Coarse finite element mesh of triaxially braided RUC; each thick shell element represents one subcell and consists of three through thickness integration points

Table 1: Summary of Unidirectional Ply Volume Fractions and Ply Thicknesses

Subcell A Layup	*Braid Angle*	*Fiber Vf (%)*	*Thickness (%)*
Braider Tow	-60°	54.4	25
Axial Tow	0°	65.6	50
Braider Tow	60°	54.4	25
Subcell B Layup	*Braid Angle*	*Fiber Vf (%)*	*Thickness (%)*
Braider Tow	-60°	49.1	25
Braider Tow	60°	49.1	50
Braider Tow	-60°	49.1	25
Subcell C Layup	*Braid Angle*	*Fiber Vf (%)*	*Thickness (%)*
Braider Tow	60°	54.4	25
Axial Tow	0°	65.6	50
Braider Tow	-60°	54.4	25
Subcell D Layup	*Braid Angle*	*Fiber Vf (%)*	*Thickness (%)*
Braider Tow	60°	49.1	25
Braider Tow	-60°	49.1	50
Braider Tow	60°	49.1	25

[a]Shown as percent of overall subcell thickness

Table 2: E862 Material Properties and Polymer Constitutive Model Parameters

Young's Modulus	*Taken from DMA data*
Poisson's Ratio	0.4
Density (g/m^3)	1.2E6
CTE (1/K)	5.4E-5
Specific Heat (J/(g-K))	1.26
D_0 (1/s)	1E6
n	0.6454
q	75.4973
α_0	0.05
α_1	0.075
$Z_0(T)$ (Pa-K)	$-(1.526E9)T + 6.8897E11$
$Z_1(T)$ (Pa-K)	$-(2.7062E9)T + 1.3332E12$

Table 3: T700 Fiber properties

Axial Young's Modulus	230 GPa
Transverse Young's Modulus	15 GPa
Axial Poisson's Ratio	0.2
Transverse Poisson's Ratio	0.3
In-Plane Shear Modulus	27 GPa

Straight-Sided Coupon Simulation Results

To verify the subcell methodology, axial and transverse straight-sided coupon tests conducted by Littell [8] were simulated and compared to experimental data. In the axial (0°) and transverse (90°) tension tests, the specimens were cut such that the axial tows were oriented parallel and perpendicular, respectively, to the loading direction. The coupons used in the experiments were 304.8 mm in length, 35.8 mm in width, 3.175 mm in thickness, and had a gage length of 203.2 mm. Each physical coupon had six through-thickness layers of triaxially braided preform. The axial and transverse coupon finite element meshes, shown in Figure 5, were spatially discretized with 1920 and 1932 thick shell elements (ELFORM=5) [33, 34], respectively, each with three through-thickness integration points and type 6 hourglass control [35]. Six thick shell elements were used through the thickness to represent each of the six layers of preform in the physical coupons. No contact was used between layers (elements of adjacent layers share nodes) and only the coupon gage sections were modeled. In the simulations, all the nodes of one end of the model were prevented from translating and rotating in all directions whereas the nodes on the other end of the coupon were only permitted move in the load direction. The nodes permitted to move in the load direction were displaced at a constant rate of 0.0106 mm/sec, the same rate used in the experiments. Due to the nominal nodal accelerations, mass scaling was used to achieve a reasonable explicit timestep. It should be noted that a mesh refinement study has not been performed in this work and that, due to the mesh density used in the current models, no through thickness nesting of axial tows could be modeled; in all models, the axial tows in each layer run parallel to and lie directly on top of each other through the thickness.

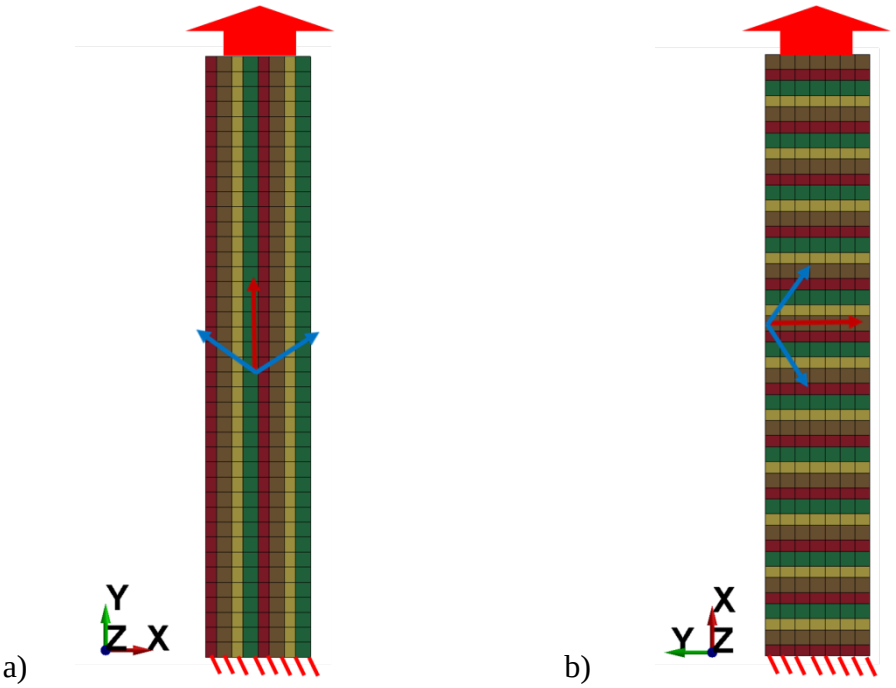

Figure 5: Finite element meshes of straight-sided a) axial and b) transverse tensile coupon gage sections.

The simulated stress-strain curves for the 0° (axial) coupon superimposed with the experimental data can be seen in Figure 6a. The predicted modulus is in excellent agreement with experimental data. It should be

noted that, since damage and failure have not yet been incorporated into the analysis, the end of the simulated stress-strain curve should not be interpreted as predicted coupon failure.

The simulated stress-strain curves for the 90° (transverse) coupon superimposed with experimental data is shown in Figure 6b. Kohlman [32] attributed the nonlinear response in the transverse tension test to damage (transverse splitting) in the axial tows, which terminate at the free edge. In the experiments, damage was found to initiate at the free edge and propagate in the direction of the bias tows [32]. Since all nonlinearity in the current methodology is due to inelasticity rather than a combination of inelasticity and damage, the nonlinearity observed in the experiment is not captured by the simulation. However, good agreement is obtained between the simulated and experimental elastic part of the stress-strain curve.

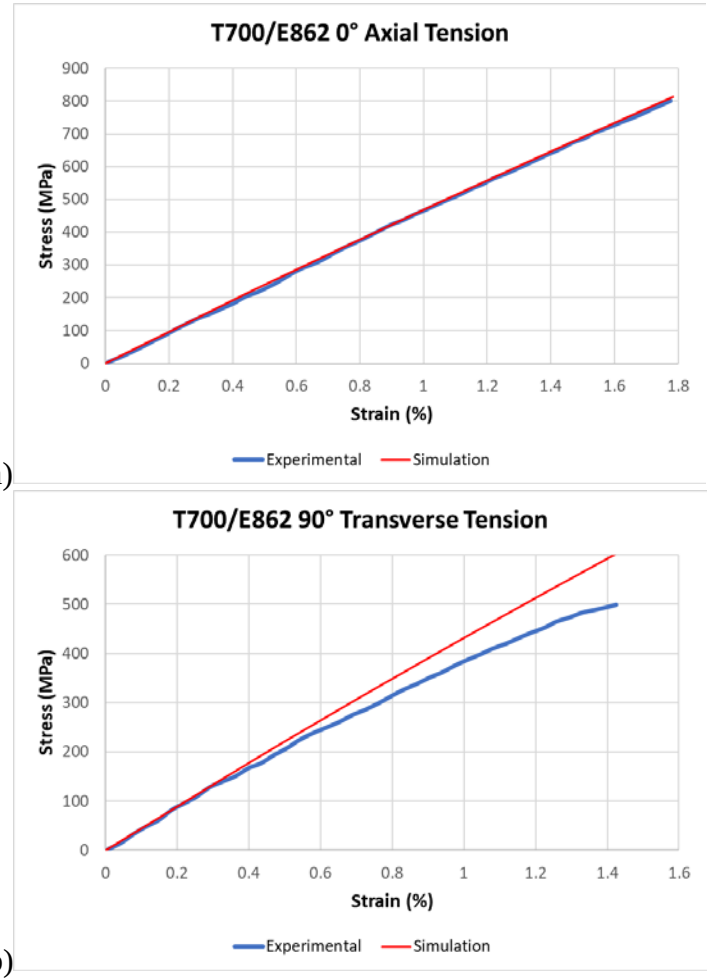

Figure 6: Stress-strain curves for straight-sided coupon simulations superimposed with experimental data [8]; (a) 0° axial tension; (b) 90° transverse tension.

Impact Simulation Results

As part of an ongoing investigation into the impact response of braided polymer matrix composite structures, a series of flat panel impact experiments have been conducted by NASA personnel on a variety of triaxially braided composite material systems at NASA Glenn Research Center according to ASTM standard D8101 [36]. The experiments consisted of impacting triaxially braided composite panels with a cylindrical, spherical nose aluminum projectile. The braided composite panels were square with side lengths of 30.48 cm

and a thickness of 3.175 mm. Panels were held in place with a circular aperture with a diameter of 25.4 cm secured by twenty-eight 9.5 mm bolts. The cylindrical section of the semi-hollow aluminum projectile had a radius of 2.53 cm and a wall thickness of 0.76 mm; the front face of the spherical nose had a radius of 3.81 cm and a nose thickness of 0.635 cm; the projectile length was 4.95 cm [10]. In the impact experiments, digital image correlation (DIC) was used to monitor the strains and displacements of a square section on the back side of the test panels with side lengths of roughly 35 mm. More details regarding the impact test setup and projectile geometry can be found in References 37 and 38.

The experimental data in this section for the T700/E862 [0°/60°/–60°] triaxially braided material system has been provided by Revilock [39, personal communication]. Since damage and failure are not currently incorporated into the analysis, simulations were conducted of an experiment for which no projectile penetration occurred and good DIC data was available. The impact velocity and initial temperature in the experiment were 160.058 m/s and 21°C, respectfully. The same impact velocity and initial temperature were used in the simulations. Like the straight-sided test coupons, the flat panels consisted of six layers of the triaxially braided perform through the panel thickness. As such, the flat panel mesh was discretized with six through thickness layers of thick shell elements with type 6 hourglass control. The panel mesh consisted of 19398 thick shell elements and can be seen in Figure 7b. A side view of the finite element mesh of the panel and the aluminum impactor are shown in Figure 7a. To simulate the 25.4 cm diameter fixture used to hold the composite panels, an SPC constraint was applied to all translational and rotational degrees of freedom of all nodes outside a 25.4 cm diameter circle; the bolts were not explicitly modeled. The aluminum projectile, which was discretized with 17760 reduced integration solid elements with standard type 1 viscous hourglass control, was set up to impact the plate at the center of the 25.4 cm diameter circle of unconstrained nodes. The *CONTACT_AUTOMATIC_SINGLE_SURFACE card was used to simulate contact between the projectile and panel meshes. The density, Young's modulus, and Poisson's ratio of the aluminum used in the simulations were 2700 kg/m^3, 74 GPa, and 0.3, respectively.

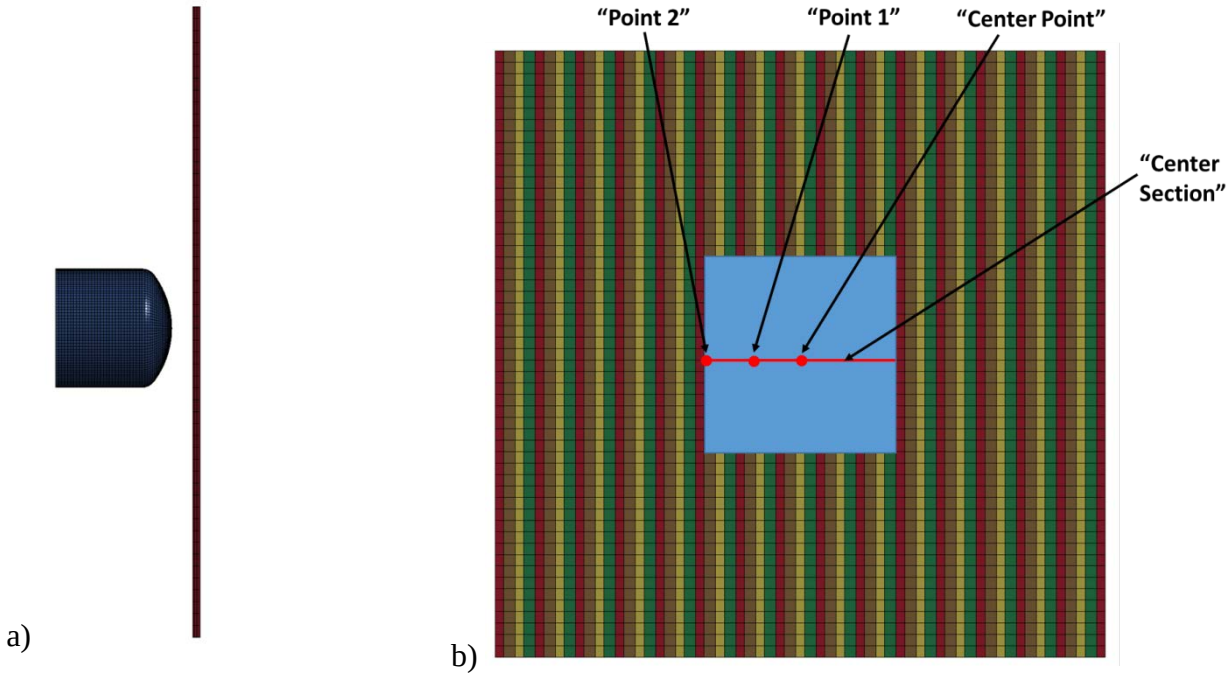

Figure 7: a) back of plate with projectile shown; b) backside of plate with DIC area, section, and points labeled.

In Figure 7b, the blue region on the panel mesh corresponds to the area on the back of the test panel monitored by DIC in the experiments. Additionally, the out of plane displacement of the points labeled “Point 1”, “Point 2”, and “Center Point”, as well as the “Center Section” are monitored during the experiments. To evaluate the effects of incorporating adiabatic heating and dynamically-calculated elastic properties (based on shifting of DMA data with integration point effective strain rate) for the polymer matrix, three different simulations were conducted and compared to each other and experimental data. The details of the three simulations are shown in Table 4. It should be noted that an inelastic heat fraction of unity implies all plastic work is dissipated in the form of heat; in this case, simulated temperature rises represent an upper bound. Additionally, in Simulation 3 (Table 4), the elastic modulus of the polymer matrix was set to the quasi-static value of 2.7 GPa; in Simulations 1 and 2, the elastic modulus of the polymer matrix in each microscale subcell is determined based on the current integration point effective strain rate and the subcell temperature using the previously described shifting methodology. The simulations will be referred to by their identification numbers listed in the first column of Table 4 for the remainder of the section.

Table 4: Details of three different impact simulations

Simulation ID #	Initial Temperature	Initial Projectile Velocity	Inelastic Heat Fraction	Elastic Properties
1	21°C	160.058 m/s	1	DMA data
2	21°C	160.058 m/s	0	DMA data
3	21°C	160.058 m/s	0	Quasi-static

Figures 8a-c show time histories of the experimental and simulated out-of-plane displacements for Point 1, Point 2, and the Center Point whereas Figure 9 shows the experimental and simulated out-of-plane displacement contours for simulation 0.00015 seconds after impact. Note that in Figure 8a, the experimental curve cuts off early due to loss of the dot pattern required by the DIC. Contours of out-of-plane displacement in Simulation 1 and the experiment 0.00015 seconds after impact also agree well, as seen in Figure 10. It is interesting to note that Simulations 1, 2, and 3 show almost identical responses in Figures 8a-c and Figure 9, despite the significant local temperature rises observed in Simulation 1, which will be discussed later. This is likely due to the fact that fiber failure is not yet incorporated into the analysis. It is expected that local thermal softening would cause nearby fibers to carry a higher load and subsequently experience an earlier failure than in the isothermal case.

a)

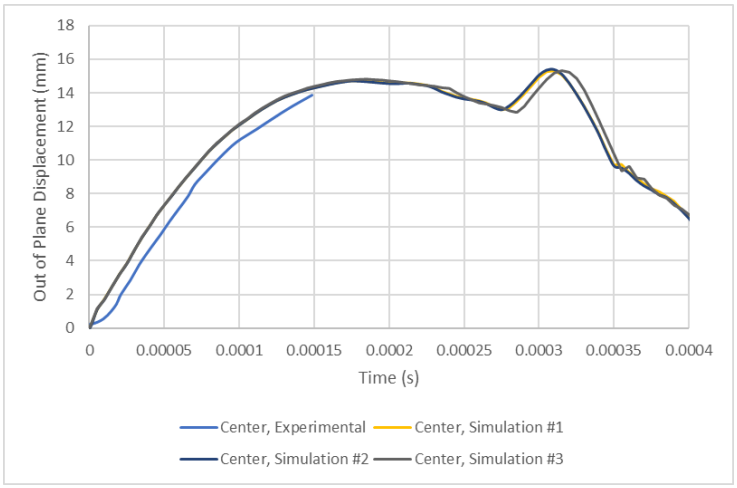

b)

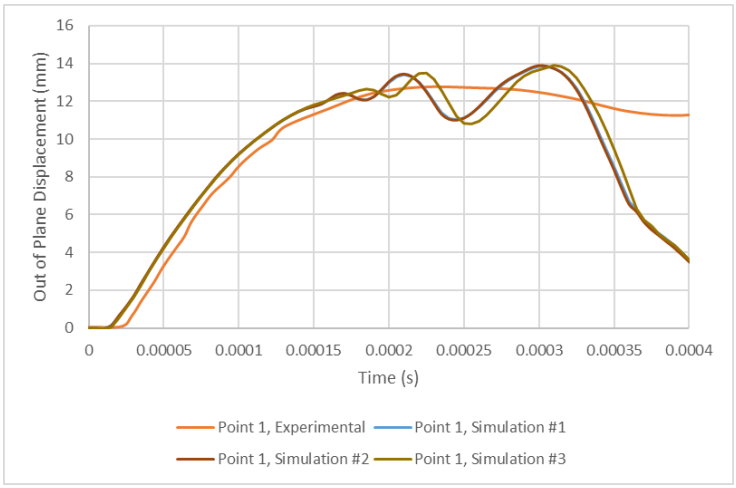

c)

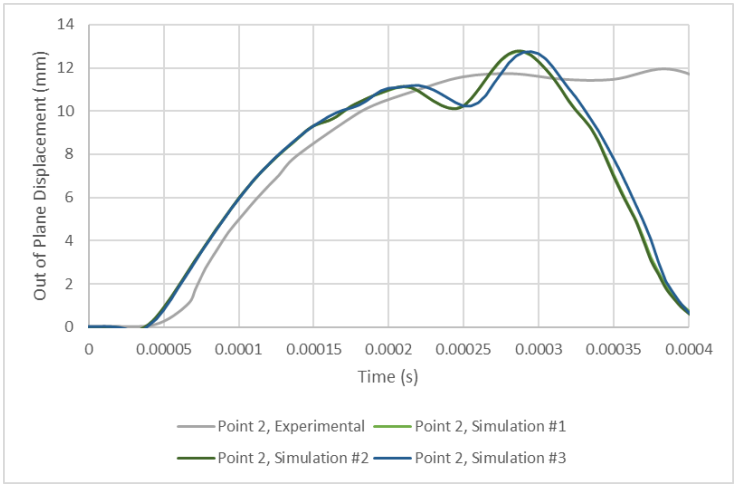

Figure 8: Out-of-plane displacement time histories for the experiment and three simulations for a) Center Point; b) Point 1; c) Point 2.

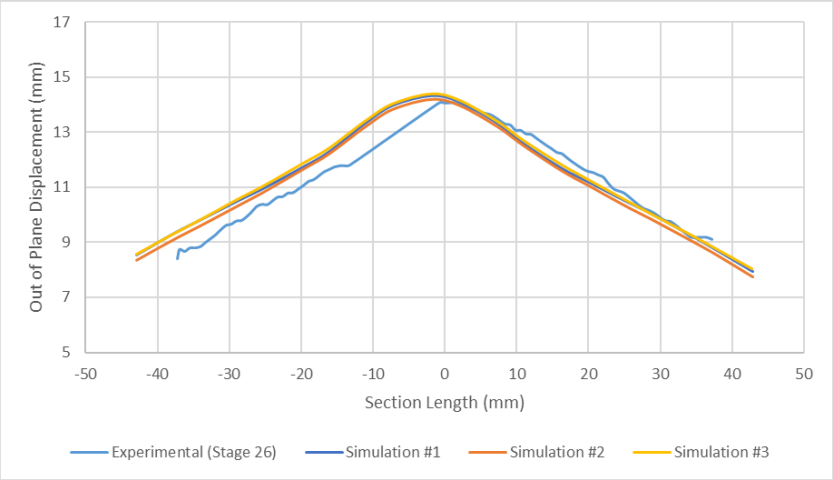

Figure 9: Experimental and Simulated out-of-plane displacement versus section length 0.00015 seconds after impact.

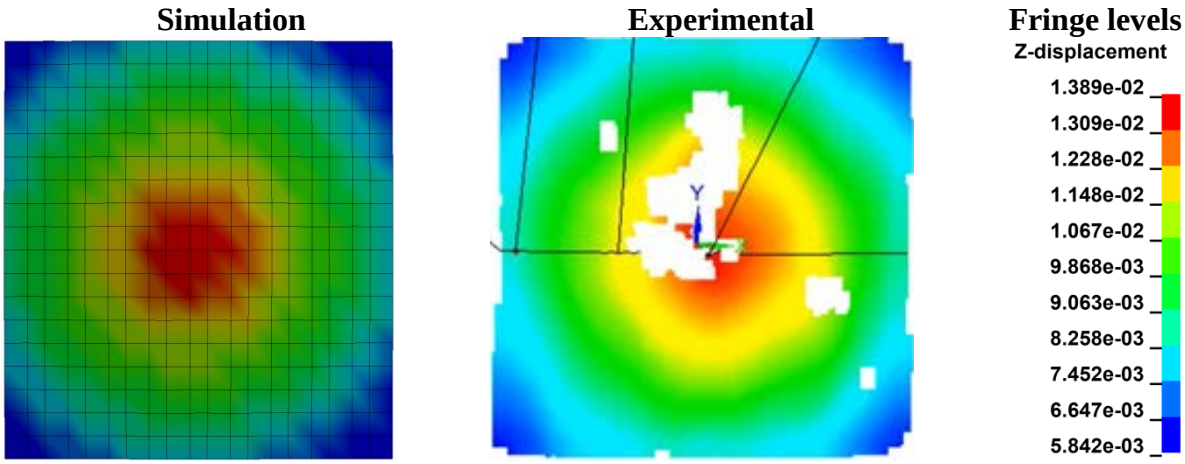

Figure 10: Simulated and experimental contours of out of plane displacement at t=0.00015 seconds for Simulation 1; Z-displacement is in meters.

Figures 11a-f show contours of the maximum value of subcell absolute temperature (Kelvin) 0.00015 seconds after impact in Simulation 1 for each of the six through thickness layers of thick shell elements. Layer 1 designates the layer impacted by the projectile whereas layer 6 denotes the backside of the plate. It is evident that the highest temperature rises occur in the middle two layers, with the the maximum temperature of 395.75 Kelvin (122.6°C) occurring in the 4th layer of thick shell elements. It should be noted the initial temperature was 21°C. It is also interesting to note that the simulation predicts higher temperature rises on the back layer than the layer the projectile comes into contact with. It is expected that, when progressive damage and failure is incorporated into the analysis, accounting for the effects of adiabatic heating in the polymer matrix will result in more accurate model predictions.

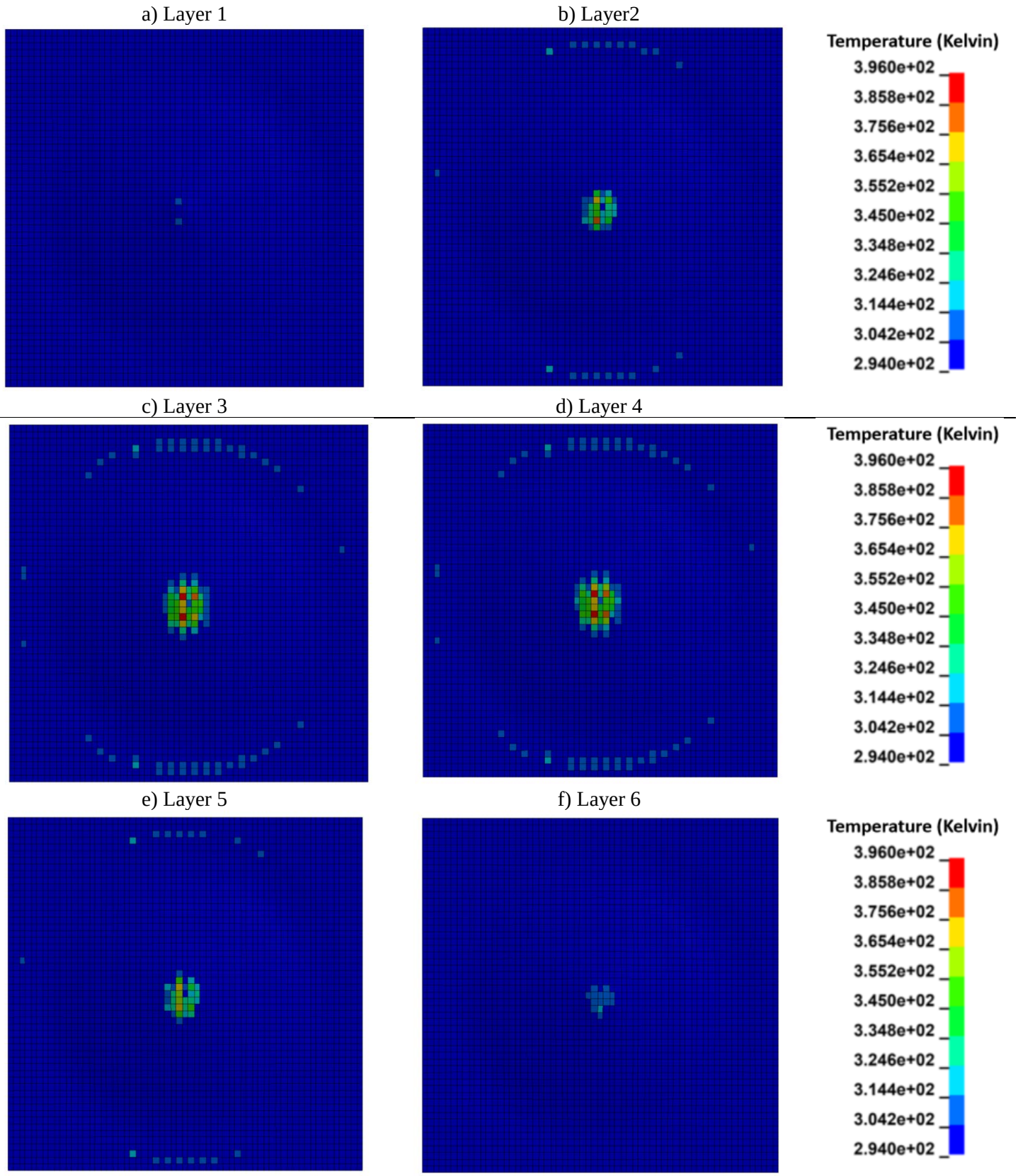

Figure 11: Contours of maximum subcell temperature rise on various layers in Simulation 1; layer 1 designates the layer impacted by the projectile whereas layer 6 denotes the backside of the plate.

Conclusion

Details regarding the development of a UMAT designed to facilitate the analysis of PMCs with complex fiber architectures subjected to ballistic impact loading conditions, including effects of adiabatic heating due to high rate inelastic deformation of the polymer matrix, have been presented. The UMAT is based on the GMC micromechanics theory and accounts for the complex interaction between fiber filaments and the strain rate, temperature, and pressure dependent polymer matrix. A nonisothermal unified viscoplastic constitutive model was employed to model the nonlinear response of the thermoset polymer matrix whereas carbon fiber filaments were assumed to be transversely isotropic and exhibit linear elastic constitutive behavior. All constitutive models were applied at the lowest (micro) length scale. Temperature rises in the polymer matrix due to the conversion of plastic work to heat were simulated at the microscale, assuming adiabatic conditions. A technique based on shifting DMA data was utilized to dynamically calculate matrix moduli at each timestep in explicit finite element simulations using the integration point effective strain rate and the microscale subcell temperature. Quasi-static straight-sided coupon tests and flat panel impact tests conducted on a representative T700/E862 [0°/60°/–60°] triaxially braided composite material system were simulated with the developed UMAT. To preserve heterogeneity at the highest length scale in finite element models, a subcell-based approach was utilized, whereby the mesoscale RUC of the triaxial braid was discretized into unique subcell regions based on the braid architecture. Simulations of straight-sided axial tension tests were in excellent agreement with experimental data whereas simulations of straight-sided transverse tensile coupon tests agreed well with the linear portion of the experimental stress-strain curve, but were unable to accurately capture the nonlinearity observed in the test. This is because the nonlinearity in the straight-sided transverse tensile coupon test was due to progressive matrix damage that initiated at the free edge. However, in the current version of the UMAT, all nonlinearity is due to inelasticity rather than a combination of inelasticity and progressive damage. To assess the manifestation of rate and temperature dependent elastic properties and matrix adiabatic heating on the impact response of the triaxially braided composite, an impact test conducted at NASA Glenn Research Center on a T700/E862 [0°/60°/–60°] triaxially braided composite panel was simulated. Three different simulation cases were considered: no adiabatic heating with quasi-static matrix moduli; no adiabatic heating with dynamically calculated matrix moduli; adiabatic heating with dynamically calculated matrix moduli. The results of the three impact simulations were very similar, likely because progressive damage and failure have not yet been incorporated into the analysis methodology. However, the adiabatic impact simulation predicted local temperature rises of approximately 100°C. It is expected that, once progressive damage and failure are incorporated into the analysis, accounting for the effects of strain rate, temperature, pressure, and adiabatic heating will play a major role in predicting the impact response of PMC structures.

Acknowledgement

This material is based upon work supported by the National Aeronautics and Space Administration under Grant Number NNX15AU36H through the NASA Harriett G. Jenkins Graduate Fellowship activity.

References

[1] Johnston, J. P., Pereira, J. M., Ruggeri, C.R., and Roberts, G. D. "High Speed Thermal Imaging on Ballistic Impact of Triaxially Braided Composites". American Society of Composites Conference Proceedings (2017). Paper #54.

[2] Chiou, S. T., Tsai, H. L., & Lee, W. S. (2007). Effects of strain rate and temperature on the deformation and fracture behaviour of titanium alloy. Materials transactions, 48(9), 2525-2533.

[3] Hallquist, J.Q., "LS-DYNA Keyword User's Manual," Volume II Material Models, Version 971, Livermore Software Technology Company, Livermore, CA, 2006.

[4] Tabiei, A., & Ivanov, I. (2002). Computational micro-mechanical model of flexible woven fabric for finite element impact simulation. International journal for numerical methods in engineering, 53(6), 1259-1276.

[5] Ivanov, I., & Tabiei, A. (2004). Loosely woven fabric model with viscoelastic crimped fibres for ballistic impact simulations. International journal for numerical methods in engineering, 61(10), 1565-1583.

[6] Cousigné, O., Moncayo, D., Coutellier, D., Camanho, P., & Naceur, H. (2014). Numerical modeling of nonlinearity, plasticity and damage in CFRP-woven composites for crash simulations. Composite Structures, 115, 75-88.

[7] Matzenmiller, A. L. J. T. R., Lubliner, J., & Taylor, R. L. (1995). A constitutive model for anisotropic damage in fiber-composites. Mechanics of materials, 20(2), 125-152.

[8] Littell, J. (2008). "The experimental and analytical characterization of the macromechanical response for triaxial braided composite materials". The University of Akron.

[9] Blinzler, B. J. (2012). "Systematic approach to simulating impact for triaxially braided composites". The University of Akron.

[10] Carney, K., Pereira, M., Kohlman, L., Goldberg, R., Envia, E., Lawrence, C., ... & Emmerling, W. (2013). Weight Assessment for Fuselage Shielding on Aircraft With Open-Rotor Engines and Composite Blade Loss.

[11] Schweizerhof, K., Weimar, K., Munz, T., & Rottner, T. (1998, September). Crashworthiness analysis with enhanced composite material models in LS-DYNA–merits and limits. In LS-DYNA World Conference, Detroit, MI (pp. 1-17).

[12] Paley, M., and J. Aboudi. "Micromechanical analysis of composites by the generalized cells model." Mechanics of materials 14.2 (1992): 127-139.

[13] Cheng, J., and Binienda, W. K., "Simplified braiding through integration points model for triaxially braided composites." Journal of Aerospace Engineering 21.3 (2008): 152-161.

[14] Li, X., Binienda W. K., and Littell, J. D., "Methodology for impact modeling of triaxial braided composites using shell elements." Journal of Aerospace Engineering 22.3 (2009): 310-317.

[15] Goldberg, R. K., Blinzler, B. J., and Binienda, W. K., "Modification of a Macromechanical Finite Element–Based Model for Impact Analysis of Triaxially Braided Composites." Journal of Aerospace Engineering (2011).

[16] Xiao, X., et al. "Strength prediction of a triaxially braided composite." Composites Part A: Applied Science and Manufacturing 42.8 (2011): 1000-1006.

[17] Cater, C. R., et al. "Single Ply and Multi-Ply Braided Composite Response Predictions Using Modified Subcell Approach." Journal of Aerospace Engineering (2014): 04014117. DOI: 10.1061/(ASCE)AS.1943-5525.0000445.

[18] Cater, C., Xiao, X., Goldberg, R. K., & Kohlman, L. W. (2015). Experimental and Numerical Analysis of Triaxially Braided Composites Utilizing a Modified Subcell Modeling Approach.

[19] Sorini, C., Chattopadhyay, A., Goldberg, R. K., & Kohlman, L. W. (2016). Development of a Subcell Based Modeling Approach for Modeling the Architecturally Dependent Impact Response of Triaxially Braided Polymer Matrix Composites.

[20] Bodner, S.R.: Unified Plasticity for Engineering Applications. Kluwer Academic/Plenum Publishers, New York, 2002.

[21] Goldberg, Robert K., Gary D. Roberts, and Amos Gilat. "Implementation of an associative flow rule including hydrostatic stress effects into the high strain rate deformation analysis of polymer matrix composites." Journal of Aerospace Engineering 18.1 (2005): 18-27.

[22] Sorini, C. W., Chattopadhyay, A., and Goldberg, R.K. "Effects of Adiabatic Heating on the High Strain Rate Deformation of Polymer Matrix Composites". American Society of Composites Conference Proceedings (2017). Paper #145.

[23] Mulliken, A. D., and M. C. Boyce. "Mechanics of the rate-dependent elastic–plastic deformation of glassy polymers from low to high strain rates." International journal of solids and structures 43.5 (2006): 1331-1356.

[24] Gilat, A., Goldberg, R. K., & Roberts, G. D. (2007). Strain rate sensitivity of epoxy resin in tensile and shear loading. Journal of Aerospace Engineering, 20(2), 75-89.
[25] Varghese, A. G., and R. C. Batra. "Constitutive equations for thermomechanical deformations of glassy polymers." International Journal of Solids and Structures 46.22 (2009): 4079-4094.
[26] Rittel, Daniel. "On the conversion of plastic work to heat during high strain rate deformation of glassy polymers." Mechanics of Materials 31.2 (1999): 131-139.
[27] Pan, Zhongxiang, et al. "Transient heat generation and thermo-mechanical response of epoxy resin under adiabatic impact compressions." International Journal of Heat and Mass Transfer 95 (2016): 874-889.
[28] Bednarcyk, B. A., & Pindera, M. J. (1997). Micromechanical modeling of woven metal matrix composites.
[29] Pindera, Marek-Jerzy, and Brett A. Bednarcyk. "An efficient implementation of the generalized method of cells for unidirectional, multi-phased composites with complex microstructures." *Composites part B: engineering* 30.1 (1999): 87-105.
[30] Bednarcyk, B. A., & Arnold, S. M. (2000). Modeling woven polymer matrix composites with MAC/GMC.
[31] Aboudi, Jacob, Steven M. Arnold, and Brett A. Bednarcyk. Micromechanics of composite materials: a generalized multiscale analysis approach. Butterworth-Heinemann, 2012.
[32] Kohlman, L.W., "Evaluation of test methods for triaxial braid composites and the development of a large multiaxial test frame for validation using braided tube specimens," Ph.D. Dissertation, Department of Civil Engineering, University of Akron, Akron, OH, 2012.
[33] Guo, Y. (2000). Eight node solid element for thick shell simulations. In 6th International LS-DYNA conference, Detroit.
[34] Chatiri, M., Güll, T., & Matzenmiller, A. (2009, May). An assessment of the new LS-DYNA layered solid element: basics, patch simulation and its potential for thick composite structure analysis. In 7th European LS-DYNA Conference, Salzburg (pp. 1-12).
[35] Belytschko, T., & Bindeman, L. P. (1993). Assumed strain stabilization of the eight node hexahedral element. *Computer Methods in Applied Mechanics and Engineering*, *105*(2), 225-260.
[36] ASTM D8101 / D8101M-17, Standard Test Method for Measuring the Penetration Resistance of Composite Materials to Impact by a Blunt Projectile, ASTM International, West Conshohocken, PA, 2017, www.astm.org
[37] Pereira, J. M., Roberts, G. D., Ruggeri, C. R., Gilat, A., & Matrka, T. (2010). Experimental techniques for evaluating the effects of aging on impact and high strain rate properties of triaxial braided composite materials.
[38] Pereira, J. M., Revilock, D. M., Ruggeri, C. R., Roberts, G. D., Kohlman, L. W., & Miller, S. G. (2016). The Effects of Hygrothermal Aging on the Impact Penetration Resistance of Triaxially Braided Composites.
[39] Revilock, D., personal communication, December 11, 2017.